Static in-tire circumferential strain signature using Rayleigh-scattering fiber optic technology : Preliminary results

Martin Fontaine, Xavier Chapeleau, Vincent Baltazart, Ivan Guéguen, Louis-Marie Cottineau, Julien Cesbron, David Bétaille, Denis Coudouel

Rethinking transport
27–30 April 2020

TRA 2020 HELSINKI

Proceedings of 8th Transport Research Arena TRA 2020, April 27-30, 2020, Helsinki, Finland

Static in-tire circumferential strain signature using Rayleigh-scattering fiber optic technology : Preliminary results

Martin Fontaine[a], Xavier Chapeleau[a], Vincent Baltazart[a], Ivan Guéguen[a], Louis-Marie Cottineau[a], Julien Cesbron[b], David Bétaille[a], Denis Coudouel[c]

[a]IFSTTAR, F-44344, Bouguenais, France
[b]IFSTTAR, CEREMA, UMRAE, F-44344 Bouguenais, France
[c]Captels, Saint-Mathieu-de-Tréviers,F-34270, France

Abstract

The paper presents both the modeling and the experiment to measure the longitudinal static strain over the inner perimeter of a tire. These measurements are expected to help at updating some unknown geometrical and mechanical parameters of tires for achieving more accurate simulations under conventional CAO software (namely, Solidworks). Compared to the literature, a distributed fiber optic sensing is used to measure the inner liner tire strain profile along the perimeter. Based on the Rayleigh scattering, this technology provides a fine spatial resolution, namely, less than 1 cm. The preliminary results show the typical Mexican-hat-like circumferential strain distribution and the contact patch length. Both quantities are shown to be related to the static load.

Keywords: Strain measurement; Fiber optic; Rayleigh scattering; Contact-patch length; Finite element modeling, static loading.

1. Introduction

Autonomous car and shared vehicle perspectives have raised challenging issues concerning intelligent tires. Monitoring tires should be crucial for vehicle safety and efficient autopilot. For years industrials and scientists have been proposed in-tire embedded sensors and studied both the static and dynamic mechanical tire behaviours. Inner liner strain has been studying to understand some of tire phenomena such as friction forces and contact patch pressure (APOLLO project, Xiong (2015), Vayalat et al. (2016)). Strain gauges (Yang (2011), Garcia-Pozuelo et al. (2017), Fiber Bragg Gauges (Breglio et al. (2017), Roveri et al. (2016)) and also capacitive sensors (Matsuzaki and Todoroki (2007)), Cao et al. (2016)) have already been implemented into tire and have shown coherent results. But, as the latter methods provide one-off strain value only, some rotation system is required to get circumference strain signature, assuming the dynamic effects like inertia are filtered out.
By contrast, this paper introduces a distributed fiber optic sensing to measure the inner strain along the tire girth. The Rayleigh scattering technology is used to achieve a fine spatial resolution, namely, less than 1 cm.
The paper is organized as follows. The simulation model is presented in the first part. Then the experimental setup in laboratory is presented along with some preliminary results. In the same part, the fiber optic sensing technology is introduced. In the final part, some numerical results are compared with experimental results. At the end, a semi-empirical model based on measurements is presented and discussed.

2. Simulations

2.1. *Profile extraction*

To model the inner strain distribution along the tire girth, the finite element software SolidWorks (SW) has been selected.
Basically, the first step for the finite element modelling (FEM) consists in the accurate geometrical design of the tire transversal profile. In Europe, tire manufacturers must respect the ETRTO external tire design specifications while keeping secret the inner profile geometry (Fig.1(a)).

a

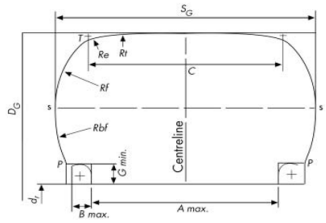

b

Fig. 1 (a) ETRTO Bounding box; (b) Tire profile cutting

Following the previous approach in Hölscher et al (2004), Yang (2011),Vayalat (2016), basic processing tools allow us to identify the different component layers of the inner tire transversal profile. We then provide in Fig.1(b) the geometry of the layers inside the tread, the undertread and the sidewall. The different geometric characteristics are finally imported into the SW FEM software.

2.2. *Mechanical properties and rheological model*

In fact, the different parts of tires, namely, sidewalls, undertread and tread, are made of various rubber types which depict specific non-linear mechanical properties and metal matrix composite material layers considered as orthotropic linear materials. Once the geometry is defined, the second step of FEM is then to fill the material with reliable rheological characteristics, i.e., the model and values. Rheological models, which correlate stress and strain values were defined according the literature review shown in Table1. As an elastomer material, hyper-elastic model is used to describe rubber behaviour. The stress law is expressed as a function of strain energy density function. This function led to several models in literature which the accuracy depends of the expected strain range.
Mooney-Rivlin model, widely used to model the strain energy density function, for tire FEM (Table1), is well suitable for elongation range until 100 %. According to the literature, inner liner elongation rate is about 1 % (10 000με). Reader can refer to Marckmann and Verron (2006) to get more information about the existing hyper-

elastic behaviour law for an incompressible and isotropic elastomer and the strain energy density function and the Mooney-Rivlin model.

The two constants C_{01} and C_{10} define the Mooney-Rivlin material properties. Layers behaviour is linear and orthotropic. Young modulus in each direction (longitudinal and transversal) are adapted from Michel (2010) and Mooney-Rivlin are adapted from Tönük and Ünlüsoy(2001). Constant values are given in Table 2. Only transversal and lateral young modulii are defined for orthotropic layers, considered as thin plates, according to the Kirchoff-Love plate theory..

Table 1. Existing FEA studies of tires under static loading

Authors	**Rubber model**	**Layers model/ Cord elements**	**Software**	**Profile extraction**	**Topic**	**Simulated data**
Helnwein et al., 1993	Mooney -Rivlin (MR)	MR +Hooke(H)	Marc MSC	n/a	Composite layers modeling	Deflection
Tönük and Ünlüsoy, 2001	MR	H	Marc MSC	n/a	Cornering forces prediction	Lateral forces
Zhang et al., 2002	MR	H	ANSYS	n/a	Stress analysis	Stress, deflection and contact pressure
Hölscher et al, 2004	MR	H	Marc MSC	Image processing	Frictional behavior	Stress, strain and deflection
Ghoreishy, 2006	MR	H	ABAQUS	n/a	Finite element method	Contact pressure and deflection
Matsuzaki and Todoroki, 2008	MR	n/a	ANSYS	n/a	Intelligent tire, Strain monitoring	Deflection, strain, contact patch length
Nguyen, 2008	MR	H	ANSYS	n/a	Tire vibrations	Resonance modes
Michel, 2010	MR	H	Altair Radioss		Pressure, fissure	Tyre burst
Matsuzaki et al., 2010	MR	H	ANSYS	n/a	Load estimation	Strain
Yang, 2011	Yeoh	H	ABAQUS	Image processing	Vehicle dynamics	Strain
Wang et al., 2013	Yeoh	H	ABAQUS	n/a	Influence of friction coefficient	Contact pressure,
Vayalat, 2016	Neo-Hookean	Neo-hookean	ABAQUS	Image processing	Contact patch characterization	Contact pressure/ dimensions
Ballo et al., 2018	MR	H	n/a	n/a	Tire-rim interaction	Deflection, rim strain

Table 2. Material tire characteristics used in this paper for mechanical tire modelling

Mooney-Rivlin component	C_{10}	C_{01}	**Poisson's ratio**	**Density (kg/m^3)**
Bead filler	14.14 MPa	21.26 MPa	0.49	1020
Sidewall	171.8 kPa	830.3 kPa		
Inner liner	140.4 kPa	427 kPa		
Tread	806.1 kPa	1.805 MPa		
Layers components	**E_L/ E_T(MPa)**	**G_{LT}**	**Poisson's ratio**	**Density(kg/m^3)**
Carcass layer	1200/ 13,3	4.438	0.46	1150

Belt layer	809/ 14.7	4.9	0.44	1150
Reinforcement layer	367/ 8.9	183.2	0.13	2014

The next step is to generate the FE model by applying boundary conditions at the interface between the different components of the 3D model. Owing to the symmetry properties in both the tire and the boundary conditions, only a quarter of the tire has been modelled.

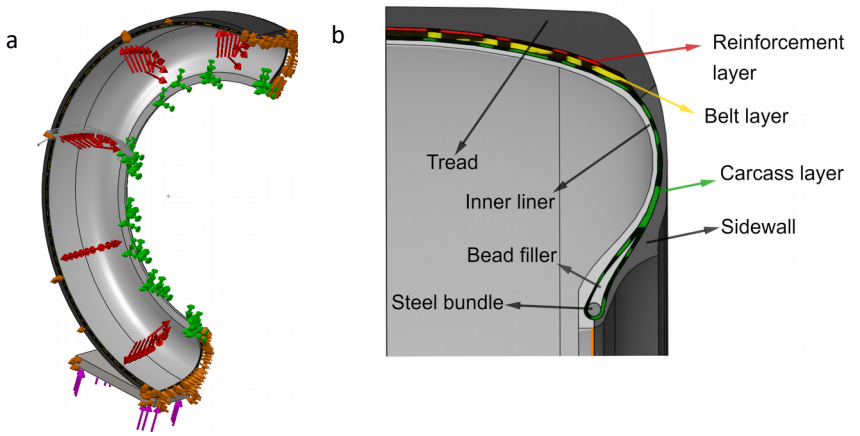

Fig. 2 (a) FEM with boundary conditions; (b) Tire cutting profile and components

The tire is laid on a rigid roughless surface. As shown in Fig. 2(a), a vertical force is applied upward on the latter surface to generate a static load on the tire, while the tire-rim interface is locked. Internal pressure is superimposed at the same time.

The meshing of the FE model is a trade-off between computer burden and accuracy requirements. Mesh element size choice mainly affects the FEA computing. To evaluate the meshing quality, mesh ratio is controlled. This ratio, between the longest and the shortest side of a mesh element is also called aspect ratio. Sharp elements with high ratio are not suitable in high stressed areas e.g bead filler. The maximum ratio has been set to 10 according SW specifications.

Finally, because the FE model is composed of different layered materials, it is required to define the contact conditions layers and rubber contacts within the tire are defined as bonded contacts. From the mesh point of view, the nodes at the interface between two materials are fixed to each other. The contact between the tire and the underlying surface is defined in SW as a non penetration contact, which allows gaps between meshes and prevents interferences between in-contact surfaces. Finally, the mesh was refined, with 1mm long mesh elements, in the central inner tire zone to provide accurate computation and to allow meaningful comparison with the FO measurements.

3. Experimental set up

3.1. Test rig and instrumentation

The experimented tire is a passenger car tire of dimensions 185/65R15 with null mileage. The optic fiber was bonded along the tire inner liner circumference (Fig.3(b)) with an appropriate bi-component epoxy glue as shown in Fig.3(c) for an optimal mechanical transfer from the tire to the sensing device. A conventional rosette strain gauge was bonded in the same way next to the fiber to serve as a reference measurement. The load is applied vertically to the latter sensor. The test rig (Fig.3(a)) is composed of a wheel which is set up on an electro-hydrostatic actuator. The wheel is also instrumented by a load cell, an actuator rod displacement sensor, a pressure sensor and a temperature sensor.

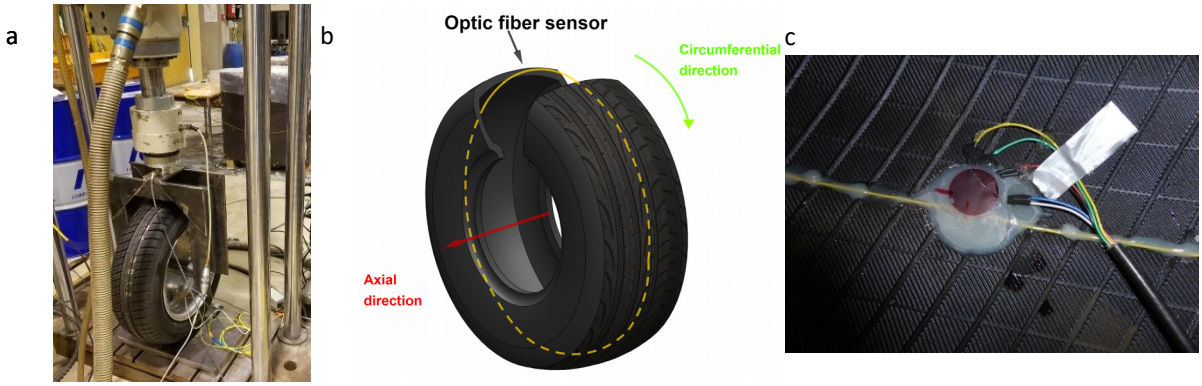

Fig. 3 (a) Test rig with the instrumented tire; (b) Representative view of the DOF inside the tire (c) Optical fiber (yellow wire) and rosette strain gauge (in purple) bonded on the inner liner of tire;

Two types of loading scenarii have been used to characterize the tire under static loading. The conventional one in Fig. 4(a) uses a step-wise increasing force to evaluate DOF sensor response and get data to compare with the FEA. The scenario in Fig.4(b) aims at testing the measurement reproducibility by a loading-unloading alternations at a fixed loading stage. For both scenarii, the peaks in force are due to a too strong force feedback.

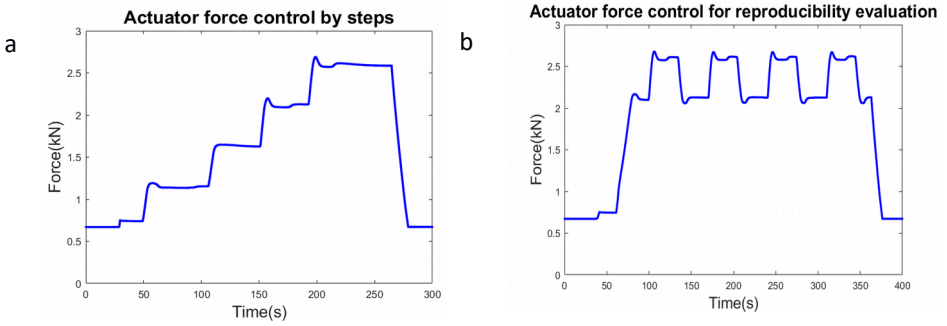

Fig. 4 (a) Step-wise increasing force command; (b) Loading-unloading alternations force command

3.2. *Distributed Optic Fiber (DOF) measuring device*

DOF Rayleigh sensing, widely used for structural health monitoring (SHM) applications, e.g., Bassil et al. (2019), is based on swept-wavelength interferometry (Froggatt and Moore (1998)). Strain and temperature generate local refractive index fluctuations on the fiber core, that induce losses by backscattering, namely, the Rayleigh scattering phenomenon. To measure the local strain (or temperature), the optical interrogator ODiSI-B powered by LUNA company compares the stressful scatter frequency profile to the stressless scatter frequency profile, namely the reference profile. The spectrum frequency shift is proportional to the local temperature and strain within the fiber, according to the following formula:

$$\Delta\nu/\nu = K_T \times \Delta T + K_\epsilon \times \Delta\epsilon \quad \textbf{(1)}$$

Where $\Delta\nu/\nu$ corresponds to the frequency shift, ΔT to the temperature variations and $\Delta\epsilon$ to the strain variations. K_T and K_ε are the corresponding proportional constants. By neglecting temperature changes, the strain value can be computed.

The fiber acts like a series of spatially distributed strain gauges. The optical interrogator enables very small spatial pitch between strain measurement, up to 0.65mm. It means that, for a one-meter long fiber sensor, more than 1500 strain values are recorded along the fiber.

Fiber sensor data are sampled at 10kHz and other sensors at 100kHz. The actuator is load-controlled to satisfy safety experimental conditions. Temperature is measured and remains steady along the experiment. The reference Rayleigh scatter frequency profile is defined for an unloaded static tire with 2 bar as internal pressure.

4. **DOF measurement results**

This section illustrates some results from the DOF sensor. The circumferential strain profile is detailed. This signature is used to determine the contact patch length w.r.t. the loading force. The main influencing physical parameters are identified.

4.1. *Circumferential strain signature*

DOF measurements provide the spatial distribution of the strain along the tire inner liner, namely, the circumferential strain signature. Both the amplitude and the shape of the spatial distribution is representative of the stress distribution caused by the vertical force on the tire structure. It is supposed to depend on the tread and layers rheological characteristics of tire. As illustrated in Fig.5.(b), the DOF signature appears as a mexican-hat-like shape.

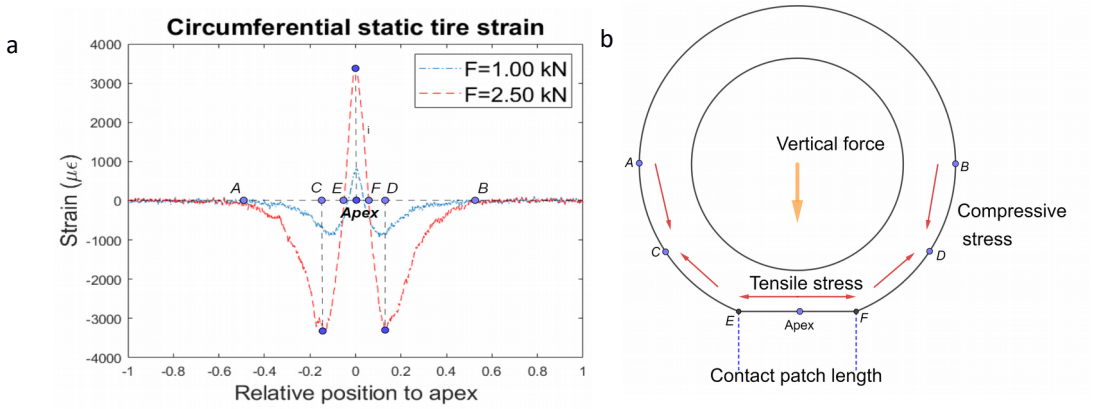

Fig. 5 (a) Static circumferential strain signature measured by DOF sensor; (b) Stress distribution over the inner liner circumference

Matching the A-E labelling between Figures 5.(a) and 5.(b), the deformation takes place in the lower part of the tire, i.e., from A to B labels. Tensile (A-E, D-B) and compressive stress (E-F) parts are observed at the central part and at the extremities of the central part, respectively. They correspond to positive and negative DOF values, respectively. The peak in compressive stress corresponds to the apex of the DOF spatial distribution; it matches to the rosette gauge values and to the experimental results published elsewhere, e.g., Matsuzaki et al (2010). Tensile and compressive stress peak values show about the same amplitude.

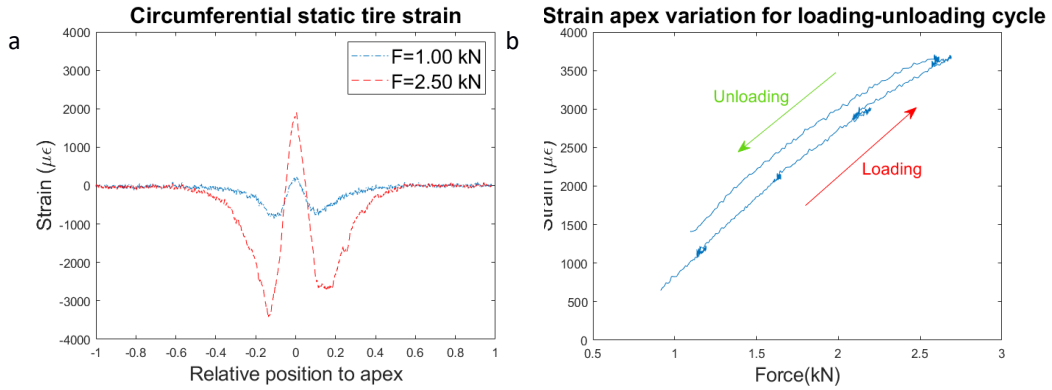

Fig. 6 (a) Asymmetric strain signature measured by DOF sensor; (b) Hysteresis phenomena over the strain apex variation

It is worth to notice that Fig.5(a) shows a symmetric strain signature because the local rubber rigidities, e.g., wear indicators included within the tire tread or periodic tread patterns, were also made symmetric w.r.t. to the vertical loading force. By contrast, Fig. 6(a). illustrates the DOF results with the opposite assumption. Besides, the apex shows a lower amplitude compared to the symmetric case. For the sake of simplicity, only the symmetrical DOF signatures have been processed in the rest of the paper. The influence of the pitch length bands has not been tested so far; it may change the rigidity along the tread as it was observed for wear indicators. Apex strain values in Fig. 6.(b) vary according to the loading and unloading phases. This hysteresis phenomena has been attributed to the rubber viscoelasticity. Internal pressure and temperature are the two other main factors that may affect the DOF signature.

4.2. Contact patch length

In this section, we propose to explore a new physical value w.r.t. to the static load. Contact patch length is representative of the interaction between the tire and the ground. According to Fig. 5.(a) and 5.(b), the latter length is defined from the zero crossing values of the DOF signature, namely, the frontier between tensile and compressive stress values. The contact patch length is then measured as the distance between E and F points in Fig. 5(a) and (b).

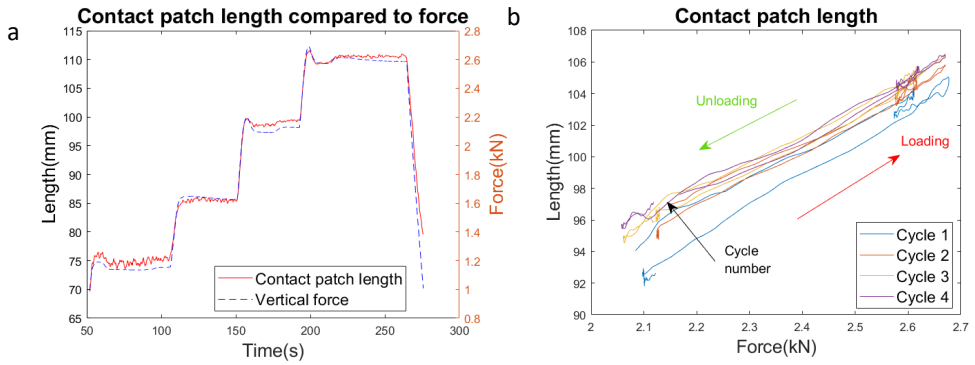

Fig. 7 (a) Contact patch length comparison with vertical force actuator command; (b) Contact patch length variation through cycles

A linear regression is observed in Fig. 7.(a) and Fig. 7.(b) between the contact patch length and the vertical force.
Through cycles, the slope remains constant. Viscoelasticity of the rubber also influences the contact patch length variations between loading and unloading cycle, and makes clearly visible the hysteresis phenomena. However, when observing successive loading- unloading steps in Fig. 7.(b), the effect phenomena seems to reduce beyond the second loading-unloading cycle. Finally, tire rigidity decreases until becoming constant at the third cycle. More cycles should be done to confirm it.

5. **Computing the circumferential static strain signature**

In this section, the FEA results are firstly exposed and compared to the measurements. The aims of this comparison is to point out some limitations of the FE modelling and then to propose some improvements. A semi empirical model is then introduced as an alternative modelling with a fewer parameters to handle compared to the FE approach. The semi-empirical modelling is expected in the future to ease the updating of the mechanical parameters of tires.

5.1. *FEA results.*

The FEM mechanical parameters exposed in Section 2 are adapted from the literature. FEA results in blue and DOF measurements in red are compared in Fig.8 in order to, in fine, improve the FEM. For both curves, a vertical force equals to 2.5kN and a 2 bar internal pressure have been set.

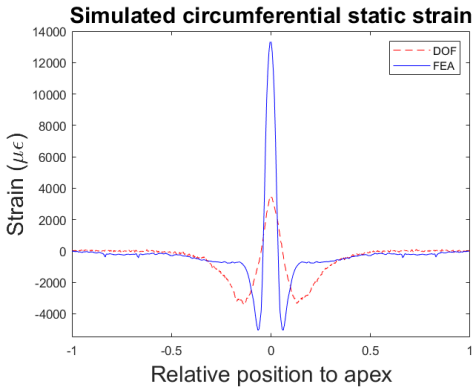

Fig. 8 Comparison of the FEA strain signature (blue curve) and the DOF measurement (red dashed curve)

Fig.8 then shows a large difference in the strain values at the apex of both curves and also in the amplitude range. Besides DOF signature shows a larger spatial spreading than the FE modelling.

All these deviations are mainly due to the tire structure rigidity. Structure rigidity is directly linked to the behavior of the tire elements. In the FEM, the behavior is defined by mechanical parameters e.g. Young modulus. In the actual FEM, the mechanical parameters, adapted from the literature, have to be updated to improve FEA accuracy. Moreover, structure rigidity is mainly ensured by the reinforcement, carcass and belt layers. To act on rigidity and the simulated strain signature, some relation have to be established between layers mechanical parameters and strain distribution and values.

5.2. Semi-empirical strain signature modelling

It is proposed to model the Mexican-hat spatial strain as the superposition of two gaussian functions as follows:

$$\varepsilon(x) = e^{\frac{-x^2}{c}}\left[1 - \frac{a}{c} * x^2\right] + \varepsilon_{Apex}\, e^{-d * x^2} - 1 \qquad \textbf{(2)}$$

where ε(x) is the strain value at the relative position to apex x. Constants a, c and d are defined according to specific values from the strain signature and are defined as follows :

$$a = \varepsilon_{Min} * e$$

$$c = \frac{-a}{(a-1)} * x_{Min}^2$$

$$d = \frac{\log(\varepsilon_{Apex})}{x_{Min}^2}$$

where ε_{Min} is the maximum compressive strain and x_{Min} the associated abscissa.

The model is computed on measured data and compared to the DOF strain signature in Fig.9. The model strain signature in dashes fits well the DOF signature along the contact patch area. Moreover the ratio between tensile and compressive values equals 1. Some deviation appears at the compressive area extremities.
Finally to make worth the semi-empirical model within the scope of the study, it will be then required to correlate the three constants (a,c and d) in Eq.2 to the mechanical parameters of the tire FEM.

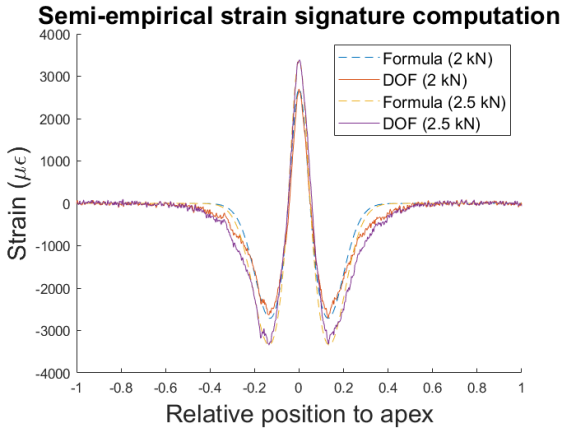

Fig. 9 Comparison of the semi empirical model (dashed curves) with the DOF measurement for 2 vertical forces

6. **Conclusion and perspectives**

This paper has presented the experiment to measure the longitudinal static strain over the inner perimeter of a tyre. Both the circumferential strain signature and the contact patch length were obtained from measurements with an optical fiber. These measurements are expected to help at updating the unknown mechanical parameters of tires for achieving more accurate mechanical simulations. Moreover a semi-empirical model has been proposed and has shown to fit to the circumferential DOF data at some extent. While not suitable for real time industrial application, DOF sensing technology is expected to provide some kind of measurement benchmark for assessment of any strain-based sensor.

References

Ballo, F., Previati, G., Gobbi, M., Mastinu, G., 2017. A Semi-Analytical Tyre Model for the Study of Tyre/Rim Interaction on a Road Vehicle, in: Volume 3: 19th International Conference on Advanced Vehicle Technologies; 14th International Conference on Design Education; 10th Frontiers in Biomedical Devices. Presented at the ASME 2017 International Design Engineering Technical Conferences and Computers and Information in Engineering Conference, American Society of Mechanical Engineers, Cleveland, Ohio, USA, p. V003T01A003. https://doi.org/10.1115/DETC2017-67730

Bassil, A., Wang, X., Chapeleau, X., Niederleithinger, E., Abraham, O., Leduc, D., 2019. Distributed Fiber Optics Sensing and Coda Wave Interferometry Techniques for Damage Monitoring in Concrete Structures. Sensors 19, 356. https://doi.org/10.3390/s19020356

Bastiaan, J.M., 2015. Design of a Smart Tire Sensor System. University of Waterloo, Waterloo, Ontario, Canada.

Breglio, G., Fienga, F., Irace, A., Russo, M., Strano, S., Terzo, M., 2017. Fiber Bragg Gratings for Strain and Temperature Measurements in a Smart Tire. WCE 2017 Vol II, 5.

Cao, S., Pyatt, S., Anthony, C., Kubba, Ammar, Kubba, Ali, Olatunbosun, O., 2016. Flexible Bond Wire Capacitive Strain Sensor for Vehicle Tyres. Sensors 16, 929. https://doi.org/10.3390/s16060929

ETRTO Standards Manual, 2005.

Froggatt, M., Moore, J., 1998. High-spatial-resolution distributed strain measurement in optical fiber with Rayleigh scatter. Applied Optics 37, 1735. https://doi.org/10.1364/AO.37.001735

Garcia-Pozuelo, D., Olatunbosun, O., Yunta, J., Yang, X., Diaz, V., 2017. A Novel Strain-Based Method to Estimate Tire Conditions Using Fuzzy Logic for Intelligent Tires. Sensors 17, 350. https://doi.org/10.3390/s17020350

Ghoreishy, M.H.R., 2006. Finite Element Analysis of the Steel-Belted Radial Tyre with Tread Pattern under Contact Load 8.

Helnwein, P., Liu, C.H., Meschke, G., Mang, H.A., 1993. A new 3-D finite element model for cord-reinforced rubber composites—Application to analysis of automobile tires. Finite Elements in Analysis and Design 14, 1–16. https://doi.org/10.1016/0168-874X(93)90075-2

Holscher, H., Tewes, M., Botkin, N., Lohndorf, M., 2004. Modeling of Pneumatic Tires by a Finite Element Model for the Development a Tire Friction Remote Sensor. Center of Advanced European Studies and Research (CAESAR), Ludwig-Erhard-Allee 2, 53175.

Marckmann, G., Verron, E., 2006. Comparison of Hyperelastic Models for Rubber-Like Materials. Rubber Chemistry and Technology 79, 835–858. https://doi.org/10.5254/1.3547969

Matsuzaki, R., Hiraoka, N., Todoroki, A., Mizutani, Y., 2010. Analysis of Applied Load Estimation Using Strain for Intelligent Tires. JMMP 4, 1496–1510. https://doi.org/10.1299/jmmp.4.1496

Matsuzaki, R., Todoroki, A., 2008. Intelligent Tires Based on Measurement of Tire Deformation. JMMP 2, 269–280. https://doi.org/10.1299/jmmp.2.269

Matsuzaki, R., Todoroki, A., 2007. Wireless flexible capacitive sensor based on ultra-flexible epoxy resin for strain measurement of automobile tires. Sensors and Actuators A: Physical 140, 32–42. https://doi.org/10.1016/j.sna.2007.06.014

Michel, L., 2010. Étude et caractérisation des phénomènes d'éclatement et d'explosion des pneus de camion. École polytechnique de Montréal, Montréal.

Nguyen, H.-H., 2008. Une nouvelle approche pour structures périodiques. Application au calcul des vibrations d'un pneumatique.

Roveri, N., Pepe, G., Carcaterra, A., 2016. OPTYRE – A new technology for tire monitoring: Evidence of contact patch phenomena. Mechanical Systems and Signal Processing 66–67, 793–810. https://doi.org/10.1016/j.ymssp.2015.06.019

Tönük, E., Ünlüsoy, Y.S., 2001. Prediction of automobile tire cornering force characteristics by finite element modeling and analysis. Computers and Structures 14.

Vayalat, T.M., 2016. Tire Contact Patch Characterization through Finite Element Modeling and Experimental Testing (Master Thesis). Virginia Polytechnic Institute and State University, Blacksburg, VA.

Wang, W., Yan, S., Zhao, S., 2013. Experimental verification and finite element modeling of radial truck tire under static loading. Journal of Reinforced Plastics and Composites 32, 490–498. https://doi.org/10.1177/0731684412474998

Xiong, Y., Tuononen, A., 2015. Rolling deformation of truck tires: Measurement and analysis using a tire sensing approach. Journal of Terramechanics 61, 33–42. https://doi.org/10.1016/j.jterra.2015.07.004

Yang, X., 2011. Finite element analysis and experimental investigation of tyre characteristics for developing strain-based intelligent tyre system (Doctoral thesis). College of Engineering and Physical Sciences of the University of Birmingham, The University of Birmingham.

Zhang, X., Rakheja, S., Ganesan, R., 2002. Stress Analysis of the Multi-Layered System of a Truck Tire. Tire Science and Technology 30, 240–264. https://doi.org/10.2346/1.2135257